The Astrophysical Journal Supplement Series, 172:86–98, 2007 September

S-COSMOS: THE *SPITZER* LEGACY SURVEY OF THE *HUBBLE SPACE TELESCOPE* ACS 2 deg^2 COSMOS FIELD I: SURVEY STRATEGY AND FIRST ANALYSIS[1]

D. B. Sanders,[2] M. Salvato,[3] H. Aussel,[2,4] O. Ilbert,[2] N. Scoville,[3,5] J. A. Surace,[6] D. T. Frayer,[6] K. Sheth,[6] G. Helou,[3,6] T. Brooke,[3] B. Bhattacharya,[6] L. Yan,[6] J. S. Kartaltepe,[2] J. E. Barnes,[2] A. W. Blain,[3] D. Calzetti,[7] P. Capak,[3] C. Carilli,[8] C. M. Carollo,[9] A. Comastri,[10] E. Daddi,[11] R. S. Ellis,[3] M. Elvis,[12] S. M. Fall,[7] A. Franceschini,[13] M. Giavalisco,[7] G. Hasinger,[14] C. Impey,[15] A. Koekemoer,[7] O. Le Fèvre,[16] S. Lilly,[9] M. C. Liu,[2,17] H. J. McCracken,[18,19] B. Mobasher,[7] A. Renzini,[13,20] M. Rich,[21] E. Schinnerer,[22] P. L. Shopbell,[3] Y. Taniguchi,[23] D. J. Thompson,[24,25] C. M. Urry,[26] and J. P. Williams[2]

Received 2006 August 28; accepted 2007 January 9

ABSTRACT

The COSMOS *Spitzer* survey (S-COSMOS) is a Legacy program (Cycles 2+3) designed to carry out a uniform deep survey of the full 2 deg^2 COSMOS field in all seven *Spitzer* bands (3.6, 4.5, 5.6, 8.0, 24.0, 70.0, and 160.0 μm). This paper describes the survey parameters, mapping strategy, data reduction procedures, achieved sensitivities to date, and the complete data set for future reference. We show that the observed infrared backgrounds in the S-COSMOS field are within 10% of the predicted background levels. The fluctuations in the background at 24 μm have been measured and do not show any significant contribution from cirrus, as expected. In addition, we report on the number of asteroid detections in the low Galactic latitude COSMOS field. We use the Cycle 2 S-COSMOS data to determine preliminary number counts, and compare our results with those from previous *Spitzer* Legacy surveys (e.g., SWIRE, GOODS). The results from this "first analysis" confirm that the S-COSMOS survey will have sufficient sensitivity with IRAC to detect $\sim L^*$ disks and spheroids out to $z \gtrsim 3$, and with MIPS to detect ultraluminous starbursts and AGNs out to $z \sim 3$ at 24 μm and out to $z \sim 1.5$–2 at 70 and 160 μm.

Subject headings: cosmology: observations — galaxies: evolution — galaxies: formation — infrared: galaxies — large-scale structure of universe — surveys

1. INTRODUCTION

The Cosmic Evolution Survey (COSMOS), covering 2 deg^2, is the first *Hubble Space Telescope* (*HST*) survey specifically designed to thoroughly probe the evolution of galaxies, AGNs, and dark matter in the context of their cosmic environment (large-scale structure) in a contiguous field that samples a volume in the high-redshift universe approaching that sampled locally by the Sloan Digital Sky Survey (SDSS). An overview of the COSMOS project, including a full characterization of the field

[1] Based on observations with the NASA/ESA *Hubble Space Telescope* obtained at the Space Telescope Science Institute, which is operated by the Association of Universities for Research in Astronomy (AURA), Inc., under NASA contract NAS 5-26555; also based on data collected at the Subaru Telescope, which is operated by the National Astronomical Observatory of Japan; the *XMM-Newton*, an ESA science mission with instruments and contributions directly funded by ESA Member States and NASA; the European Southern Observatory under Large Program 175.A-0839, Chile; Kitt Peak National Observatory, Cerro Tololo Inter-American Observatory, and the National Optical Astronomy Observatory, which are operated by AURA under cooperative agreement with the National Science Foundation; the National Radio Astronomy Observatory, which is a facility of the National Science Foundation operated under cooperative agreement by Associated Universities, Inc.; and the Canada-France-Hawaii Telescope (CFHT) with MegaPrime/MegaCam operated as a joint project by the CFHT Corporation, CEA/DAPNIA, the National Research Council of Canada, the Canadian Astronomy Data Centre, the Centre National de la Recherche Scientifique de France, TERAPIX, and the University of Hawaii.

[2] Institute for Astronomy, 2680 Woodlawn Drive, University of Hawaii, Honolulu, HI 96822; sanders@ifa.hawaii.edu.

[3] California Institute of Technology, MS 105-24, 1200 East California Boulevard, Pasadena, CA 91125.

[4] CNRS, AIM-Unité Mixte de Recherche CEA-CNRS-Université Paris VII-UMR 7158, F-91191 Gif-sur-Yvette, France.

[5] Visiting Astronomer, University of Hawaii, 2680 Woodlawn Drive, Honolulu, HI 96822.

[6] *Spitzer* Science Center, MS 314-6, California Institute of Technology, Pasadena, CA 91125.

[7] Space Telescope Science Institute, 3700 San Martin Drive, Baltimore, MD 21218.

[8] National Radio Astronomy Observatory, P.O. Box O, Socorro, NM 87801-0387.

[9] Department of Physics, ETH Zurich, CH-8093 Zurich, Switzerland.

[10] INAF-Osservatorio Astronomico di Bologna, Via Ranzani 1, I-40127 Bologna, Italy.

[11] National Optical Astronomy Observatory, P.O. Box 26732, Tucson, AZ 85726; currently at Laboratoire AIM, CEA/DSM-CNRS-Université Paris Diderot, DAPNIA/SAp, Orme des Merisiers, F-91191 Gif-sur-Yvette, France.

[12] Harvard-Smithsonian Center for Astrophysics, 60 Garden Street, Cambridge, MA 02138.

[13] Dipartimento di Astronomia, Università di Padova, Vicolo dell'Osservatorio 2, I-35122 Padua, Italy.

[14] Max Planck Institut für Extraterrestrische Physik, D-85478 Garching, Germany.

[15] Steward Observatory, University of Arizona, 933 North Cherry Avenue, Tucson, AZ 85721.

[16] Laboratoire d'Astrophysique de Marseille, BP 8, Traverse du Siphon, F-13376 Marseille Cedex 12, France.

[17] Alfred P. Sloan Research Fellow.

[18] Institut d'Astrophysique de Paris, UMR7095 CNRS, Universitè Pierre et Marie Curie, 98 bis Boulevard Arago, 75014 Paris, France.

[19] Observatoire de Paris, LERMA, 61 Avenue de l'Observatoire, F-75014 Paris, France.

[20] European Southern Observatory, Karl-Schwarzschild-Strasse 2, D-85748 Garching, Germany.

[21] Department of Physics and Astronomy, University of California, Los Angeles, CA 90095.

[22] Max Planck Institut für Astronomie, Königstuhl 17, Heidelberg, D-69117, Germany.

[23] Physics Department, Graduate School of Science, Ehime University, 2-5 Bunkyo-cho, Matuyama, 790-8577, Japan.

[24] Caltech Optical Observatories, MS 320-47, California Institute of Technology, Pasadena, CA 91125.

[25] Large Binocular Telescope Observatory, University of Arizona, 933 North Cherry Avenue, Tucson, AZ 85721.

[26] Department of Astronomy, Yale University, P.O. Box 208101, New Haven, CT 06520-8101.

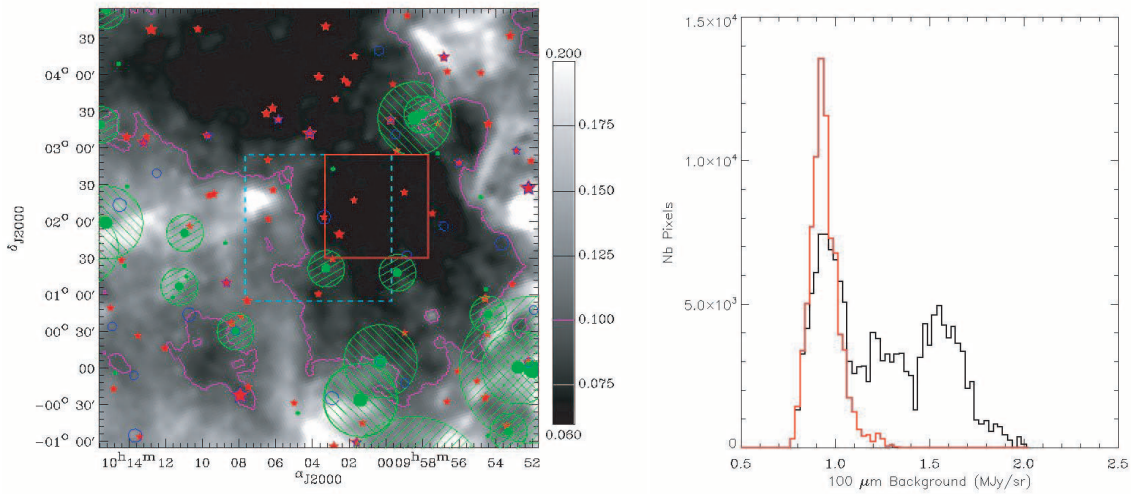

FIG. 1.—*Left*: Layout of the COSMOS Field on a map of extinction computed from the reddening map of Schlegel et al. (1998). The COSMOS field is indicated by the red rectangle ($1.41^\circ \times 1.41^\circ$) fully enclosing all of the ACS imaging, which has lower-left and upper-right corners (R.A., decl. J2000.0) at (150.7988°,1.5676°) and (149.4305°, 2.8937°). The dashed blue box represents the $2^\circ \times 2^\circ$ VVDS field. Tycho-2 bright stars are indicated by red stars. Bright NVSS radio sources are indicated by green dots. Radio sources with $S_{1.4\ \mathrm{GHz}} > 1$ Jy, 0.5–1.0 Jy, and 0.25–0.5 Jy are surrounded by hatched area circles of radius 1.5°, 1°, and 0.5°, respectively. *ROSAT* All-Sky Survey Bright Source Catalog sources are indicated by blue circles. The purple contour represents an extinction value of $A_V = 0.1$. *Right*: Histogram of the distribution of 100 μm *IRAS* emission over the entire 2 deg^2 COSMOS field (*red line*) compared to the larger VVDS field (*black line*).

and a description of the vast amount of multiwavelength data which have been, and will be, assembled is given by Scoville et al. (2007).

The COSMOS *Spitzer* (S-COSMOS) deep IRAC and MIPS data are critical to address two major goals of the COSMOS survey: the stellar mass assembly of galaxies (primarily from IRAC), and a full accounting of the luminosity from dust-embedded sources such as merging starburst galaxies and AGNs (MIPS and IRAC). IRAC measures the light from long-lived stars in galaxies over the redshift range $0.5 < z < 6$ (e.g., Mobasher et al. 2005). With morphological information from the *HST* ACS imaging, we will be able to determine how the mass assembly depends on morphological type, environment, and redshift, in addition to other properties such as X-ray and radio emission. IRAC data are also critical for determining accurate photometric redshifts for galaxies at $z > 1$ (e.g., Rowan-Robinson et al. 2005), where the peak of the stellar light has been redshifted into the IRAC bands. MIPS observations allow a determination of the total star formation rate (SFR) without requiring large corrections for extinction in galaxies, and will be used to quantify the connection between the SFR and the merger/interaction rate (e.g., Kartaltepe et al. 2007; Kampczyk et al. 2007) and the dependence on clustering environment (derived from spectroscopic and photometric redshifts). Deep COSMOS radio images (Schinnerer et al. 2007) will also be used to provide a secondary calibration of SFRs. In addition, both IRAC and MIPS probe the wavelength range where obscured AGNs have much of their bolometric luminosity. If the AGNs are heavily obscured, they may be missing from the COSMOS *XMM-Newton* survey, which is the primary basis for AGN selection (Impey et al. 2007), but they will appear in the catalogs of infrared point sources. Mid-infrared selection has been shown to be ~60% more efficient in selecting highly obscured AGNs (Polletta et al. 2006). The COSMOS field, with its size, deep mid-IR coverage, and extensive UV, X-ray, radio, and optical data sets, offers the possibility to both significantly improve the constraint on the surface density of obscured AGNs and to improve our understanding of their spectral energy distributions (SEDs).

This paper presents the infrared properties of the COSMOS field, summarizes our mapping strategy, and presents the initial quick-look results from our Cycle 2 Legacy observations, all of which were completed during the 2005 December–2006 January visibility window. Section 2 briefly summarizes the general properties of the COSMOS field (e.g., location, expected infrared backgrounds), and § 3 lays out the mapping strategy used to obtain coverage of the full field with both the IRAC and MIPS cameras. The methods used to reduce our Cycle 2 data are presented in § 4. Section 5 presents results from our preliminary analysis of the Cycle 2 data, including measured background levels and sensitivities, preliminary number counts, and asteroid detections. Our future science goals are summarized in § 6.

2. FIELD CHARACTERIZATION

2.1. *Field Location*

The COSMOS field is equatorial to ensure coverage by all astronomical facilities (centered at J2000.0 R.A. = $10^{\mathrm{h}}00^{\mathrm{m}}28.6^{\mathrm{s}}$, decl. = $+02^\circ12'21.0''$). Our field was chosen to be devoid of bright X-ray, UV, and radio sources. The time requirements for imaging over a total area of 2 deg^2 and ground-based spectra of 50,000 galaxies at $I_{\mathrm{AB}} < 25$ mag makes it strategically imperative that the field be readily observable now and in the future by all large optical/IR telescopes and especially all unique astronomical instruments (e.g., the Atacama Large Millimeter/submillimeter Array [ALMA], Extended Very Large Array [EVLA], Square Kilometer Array [SKA], Thirty Meter Telescope [TMT], and James Clerk Maxwell Telescope [JCMT] SCUBA2).

2.2. *IR Backgrounds*

The COSMOS field was chosen to have among the lowest (and most uniform) mean *IRAS* 100 μm background level for an equatorial field of its size. Figure 1 shows the field outline (*left panel*, *red square*; see caption for details) superimposed on a map of extinction computed from the reddening map of Schlegel et al. (1998), illustrating the apparent lack of contamination from foreground Galactic plane dust clouds, as well as the lack of any

strong radio and X-ray sources which could compromise deep radio and X-ray observations of the field. Figure 1 also shows in histogram form the distribution of 100 μm *IRAS* pixels within the COSMOS field versus the larger surrounding VVDS field. The sharp peak near 0.9 MJy sr^{-1}, and the lack of the higher background tail that plagues the larger VVDS region (Fig. 1, *left*, *dashed blue box*), illustrates the choices made in shifting the final COSMOS field center to truly minimize the far-infrared background levels.

Although lower background fields at higher declination and higher ecliptic latitude will have slightly better sensitivities for an equal amount of integration time, these fields suffer the major deficiency that they are not readily accessible by all unique facilities, most importantly the (E)VLA and future ALMA, which are vital for multiwavelength studies, and the future 30 m optical telescope which is likely to be unique. We believe that the accessibility to all instruments far outweighs the relatively small loss ($\sim$35%) in sensitivity for *Spitzer* observations of the COSMOS field.

3. OBSERVING STRATEGY

Because the COSMOS *HST* field is close to the ecliptic, the orientation of the detectors is always the same to within a few degrees. This allowed the specification of a maximally efficient tiling strategy, since we could accurately predict the orientation of the detectors. Neither of the mapping options available in the astronomical observation template allowed us the flexibility to tile, given the fact that the COSMOS ACS data are aligned along the right ascension and declination coordinate axes; therefore, the fields have instead been placed using the "cluster offset" option.

3.1. *Cycle 2: IRAC-Deep Coverage*

The IRAC camera has two fields of view (FOVs), each one dedicated to two channels: one for the 3.6 and 5.6 μm detectors, and one for the 4.5 and 8.0 μm detectors. The two FOVs are separated on the sky by 7′. In order to fully cover the COSMOS ACS field at nominal depth with all four IRAC bands, we had to map a slightly larger region of the sky, as shown in Figure 2.

The following four constraints dictated our final choice for the map tiling. (1) The maximum size of an IRAC astronomical observation request (AOR) is 6 hr, and in practice must be less than 5 hr. (2) Because the COSMOS *HST* field is near the ecliptic plane, asteroids were expected to be a significant contaminant. We required multiple epochs separated by 1–2 hr for asteroid rejection; in addition, each epoch had to have enough redundancy to allow for cosmic ray rejection. (3) Each epoch had to have at least 4–5 dithers per point on the sky for adequate redundancy when reducing the data. A total of four epochs were observed. (4) IRAC has two FOVs separated by 7′. The orientation of the FOVs was dictated by the orientation of the spacecraft on the day of the observation. Both FOVs had to observe the entire field.

The basic parameters of the tiling are a 4×4 grid of AORs, where each AOR is composed of a grid of 5×5 IRAC FOVs. Each AOR in the 4×4 grid was repeated sequentially three times, resulting in three individual epochs separated by a few hours. The east and south edges are trimmed to match the COSMOS *HST* field boundary. The fields overlap by tens of arcseconds, and are highly dithered. Each epoch was further offset by half an array width relative to its predecessor in order to ensure an even higher number of total dither positions in the final co-addition of all epochal data in order to minimize array-position-dependent calibration effects. Figure 2 shows the final area coverage resulting from our tiling strategy for the two IRAC FOVs. The total time for the IRAC-deep full-field mapping observations (all carried out in Cycle 2) was 166 hr. Coordinates for the Cycle 2 mapping grids are given in Table 1.

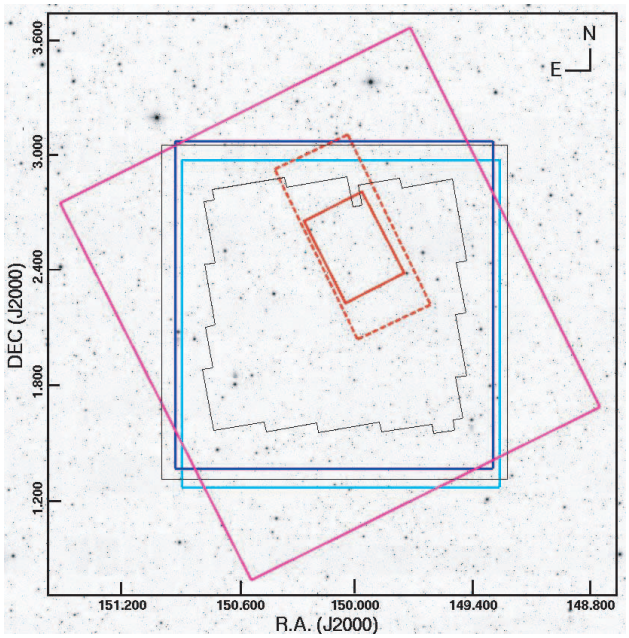

FIG. 2.—Visualization of the S-COSMOS Cycle 2 IRAC and MIPS AOR coverage. The background image is from the SDSS. *Thin black square*, CFHT *I* band; *thick black polygon*, ACS *i* band; *magenta square*, MIPS-shallow; *dashed red rectangle*, MIPS-deep test area coverage at 24 μm; *solid red rectangle*, MIPS-deep test area with coverage in all three bands; *blue square*, IRAC 3.6 μm, 5.4 μm; *cyan square*, IRAC 4.5 μm, 8.0 μm. Coordinates of the corners of each box are listed in Table 1.

1. A summary of the IRAC-deep scan map is as follows:
   3 epochs, separated by 4–5 hr each (2006 January 1–15)
   12 pointings of 100 s each
   Total depth = 1200 s
   Total time = 166 hr.

In addition, the MIPS-shallow scan map is summarized as follows:

2. 1 epoch (2006 January)
   Total depth = 80 s (24 μm), 40 s (70 μm), 8 s (160 μm)
   Total time = 16.6 hr.

Finally, a summary of the MIPS-deep test area scan map is as follows:

3. 1 epoch (2006 January)
   Total depth = 3200 s (24 μm), 1560 s (70 μm), 320 s (160 μm)
   Total time = 41.6 hr.

3.2. *Cycle 2: MIPS Coverage*

In Cycle 2, a total of 58.2 hr were allocated for MIPS observations of the COSMOS field. The entire field was mapped at a shallow depth to check for possible cirrus structure within the COSMOS field, and deep observations over a small $30' \times 20'$ region were carried out to quantify the ability of *Spitzer* to integrate down within the COSMOS field (see solid red line in Fig. 2). The data were taken in MIPS scan mode with 148″ cross-scan offsets between the forward and return scan legs. The shallow observations were taken at the medium scan rate with 1.75° scan legs.

TABLE 1
COORDINATES FOR S-COSMOS OBSERVATIONS IN CYCLE 2 AND CYCLE 3[a]

	Bottom Left		Top Left		Top Right		Bottom Right	
Field	R.A. (J2000.0)	Decl. (J2000.0)	R.A. (J2000.0)	Decl. (J2000.0)	R.A. (J2000.0)	Decl. (J2000.0)	R.A. (J2000.0)	Decl. (J2000.0)
IRAC 3.6/5.8.....	10 03 45	01 23 14	10 03 45	03 04 43	09 57 10	03 04 43	09 57 11	01 23 14
IRAC 4.5/8.0.....	10 03 36	01 17 38	10 03 36	02 58 53	09 57 03	02 58 53	09 57 03	01 17 38
MIPS-deep	10 00 14	02 14 35	10 01 04	02 40 11	09 59 53	02 49 29	09 59 02	02 23 13
MIPS-shallow.....	10 02 10	00 48 57	10 06 07	02 45 33	09 58 53	03 39 43	09 54 59	01 42 34
MIPS 24 (1).....	10 02 34	01 00 37	10 04 54	02 49 46	09 58 24	03 18 15	09 55 57	01 43 03
MIPS 24 (2).....	10 02 04	00 59 13	10 05 20	02 42 46	09 59 08	03 26 25	09 56 06	01 29 17
MIPS 70 (1).....	10 02 47	01 11 06	10 05 05	02 59 06	09 58 41	03 30 09	09 56 21	01 41 25
MIPS 70 (2).....	10 01 45	00 48 43	10 04 58	02 31 48	09 58 47	03 15 13	09 55 35	01 31 37
MIPS 160 (1).....	10 02 26	00 54 47	10 04 40	02 39 16	09 58 13	03 09 09	09 55 59	01 23 13
MIPS 160 (2).....	10 02 23	01 09 14	10 05 29	02 48 08	09 59 18	03 31 47	09 56 12	01 51 41

NOTE.—Units of right ascension are hours, minutes, and seconds, and units of declination are degrees, arcminutes, and arcseconds.
[a] Cycle 2 coordinates are given in rows 1–4. Cycle 3 coordinates are given in rows 5–10, where (1) and (2) refer to the different spacecraft orientations in 2006 January and May, respectively. The layout of the Cycle 2 and Cycle 3 maps can be seen in Fig. 2 and Fig. 3, respectively.

These shallow observations cover $1.75^\circ \times 1.97^\circ$ to a depth of 80, 40, and 8 s for the 24, 70, and 160 μm arrays, respectively.

The MIPS-deep "test area" observations were taken at the slow scan rate with 0.5° scan legs. These deep observations cover $0.5^\circ \times 0.33^\circ$ to a depth of approximately 3200, 1560, and 320 s for the 24, 70, and 160 μm arrays, respectively. The small "test area" was mapped 15 times using dithers between each map to account for the bad blocks within the 70 and 160 μm arrays and to spread out the overlapping 24 μm coverage uniformly over the field. Both forward and reverse scan mapping were done to help characterize any long-term transients as a function of scan direction.

3.3. *Cycle 3: MIPS-Deep Coverage of the Full Field*

In Cycle 3, 396.2 hr have been allocated for deep MIPS observations covering the full COSMOS field. These observations will be taken in two epochs (2007 January and 2007 May) to help minimize the zodiacal background and thus to maximize the achieved sensitivity. The observations during the two epochs will of necessity have different instrumental orientations (see Fig. 3). The field will be fully mapped 13 times at the slow scan rate with 148″ cross-step offsets between the adjacent 1.5° scan legs. The field will also be mapped once at the medium scan rate to confirm the consistency of the calibration between the Cycle 2 and Cycle 3 data sets for the same integration time. The Cycle 3 observations will cover $1.5^\circ \times 1.64^\circ$ to a depth of approximately 2800, 1400, and 280 s for the 24, 70, and 160 μm arrays, respectively (see Fig. 3).

4. DATA REDUCTION (CYCLE 2)

4.1. *IRAC*

The S-COSMOS data were initially processed by the *Spitzer* Science Center[27] (SSC). The SSC provides the Basic Calibrated Data (BCD) product, which is a set of raw scientific exposures that are flux calibrated and corrected for well-understood instrumental signatures. These include dark subtraction, linearization, and flat-fielding. After receipt of the BCD images, S-COSMOS further processes them using a data pipeline adapted from the SWIRE project and described by J. A. Surace et al. (2007, in preparation). This pipeline fixes numerous additional instrumental effects such as muxbleed, jailbarring, muxstripe, banding, and column pull-up and pull-down. It applies a frame-by-frame background correction for fluctuating bias levels. It corrects both long- and short-term image latents, and masks stray light and filter ghosts. Finally, it applies a correction for the known array-position-dependent calibration gain factors.

One caveat of this processing, which is true for all IRAC observations, is that the background on 5′ and larger scales is fixed to a *COBE*-derived background model. Operated in a shutterless mode, IRAC cannot provide an absolute measure of the sky background.

Once the frame-level images are prepared, they are reprojected to a common-tangent projection and co-added using the SSC MOPEX software[28] (Makovoz et al. 2005) to create the final

[27] See http://ssc.spitzer.caltech.edu/.

[28] See http://ssc.spitzer.caltech.edu/postbcd/.

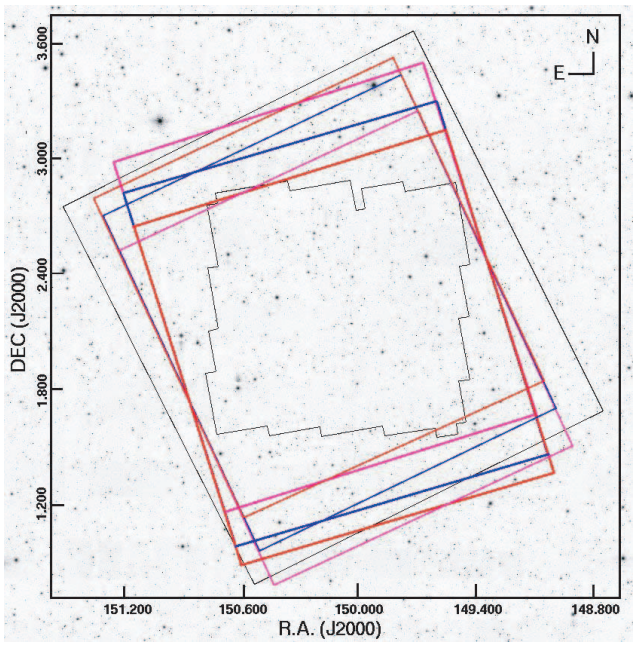

FIG. 3.—Visualization of the Cycle 3 MIPS-deep coverage of the COSMOS field. The thin black ACS and MIPS-shallow Cycle 2 observations are as in Fig. 2. The blue, magenta, and red boxes are respectively, the 24, 70, and 160 μm observations to be obtained in Cycle 3. The two "sets" of boxes represent the two different spacecraft orientations for the two epochs. Coordinates of the corners of each box are listed in Table 1.

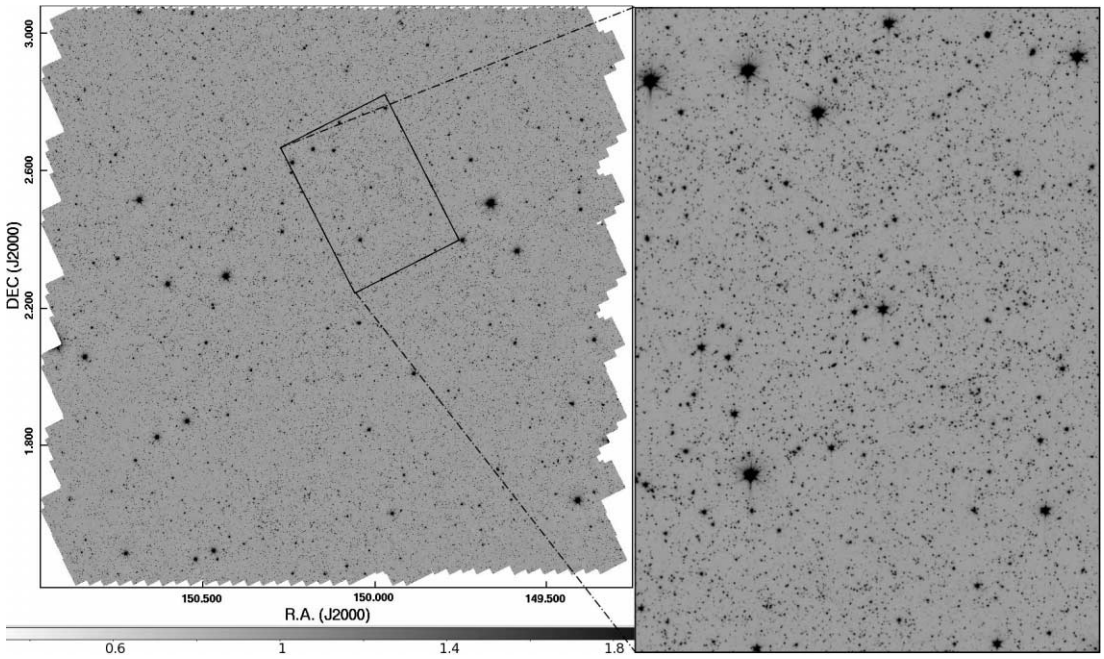

FIG. 4.—*Left*: Mosaic of IRAC 3.6 μm Cycle 2 data for the whole S-COSMOS field. *Right*: Zoomed area corresponding to the location of the MIPS-deep test area shown for comparison with Fig. 5 (*right*). The intensity scale bar is in units of μJy.

mosaicked image. An example of the quality of the data can be seen in Figure 4 (*left panel*), where the whole mosaic is shown. The zoomed area (*right panel*) better illustrates the large space density of 3.6 μm sources, and also shows that there are no obvious artifacts in the reduced image.

This reprojection also corrects for known image distortion. Since the BCD images are aligned to 2MASS, the final mosaics are also on the 2MASS astrometric solution, and generally have an accuracy of $\sim 0.2''$. Typical depth of coverage is between 12×100 and 22×100 s images per point on the sky. This is sufficient redundancy to reject cosmic rays with very high confidence. In general, asteroids are also rejected (since they move between observation epochs). Although some low-sigma residuals from slow-moving objects remain, these are easily identified by their color.

4.2. *MIPS*

The MIPS 24 μm data have been reduced using a combination of our own developed IDL routines and MOPEX (Makovoz et al. 2005). Our starting point is the BCD products generated by the SSC pipeline version S13.2, in which the data are flux calibrated. Great attention has been given to the subtraction of the zodiacal background, the dominant source of diffuse emission at 24 μm at the ecliptic latitude of S-COSMOS. Our goal was to check for the presence of weak-structured cirrus emission in the COSMOS field. Therefore, we avoided using any background subtraction method that could lower or cancel the signal from the interstellar medium (ISM). Given the large size of the field, the zodiacal background to the detectors varies across the field, from 36.8 to 37.8 MJy sr^{-1}, primarily as a function of the ecliptic latitude, but also as a function of the ecliptic longitude and of the MIPS scan mirror position. These values are slightly higher than the ones predicted by SPOT, as seen in Table 2. This excess of zodiacal background is due to the presence of dust lanes that are not included in the model that SPOT uses for its background estimation (W. T. Reach 2006, private communication). Following Fadda et al. (2006), we first subtracted the variations due to the scan mirror by identifying the sets of images taken at the same position and then determining the amount of variation due to the mirror position. We then subtracted the ecliptic background.

TABLE 2

FIELD COMPARISON OF IR BACKGROUNDS, AND SENSITIVITIES WITH PREDICTED AND MEASURED S-COSMOS CYCLE 2 IRAC-DEEP AND MIPS-DEEP OBSERVATIONS

	8.0 μm (SPOT)		24 μm (SPOT)		100 μm (*IRAS*)
FIELD	Bkg (MJy sr^{-1})	S(1200 s) (μJy)	Bkg (MJy sr^{-1})	S(3200 s) (mJy)	Bkg (MJy sr^{-1})
COSMOS[a]	6.7	14.6	31	0.065	0.90
LH, CDF-S[a]	5.2	12.7	19	0.053	0.45
SWIRE-*XMM-Newton*[a]	7.1	14.8	31	0.065	1.25
COSMOS[b]	6.9	14.6	37	0.071	0.90

[a] Total backgrounds predicted by SPOT at 8 and 24 μm are given for the different fields in the first three rows. Sensitivities (5 σ) were computed assuming 1200 s of integration with IRAC and 3200 s with MIPS, equivalent to our Cycle 2 integration times for IRAC and MIPS-deep, respectively. All *IRAS* 100 μm values are actual measurements from the *IRAS* maps.

[b] Measured median background levels over the full 2 deg^2 COSMOS field in our S-COSMOS Cycle 2 data.

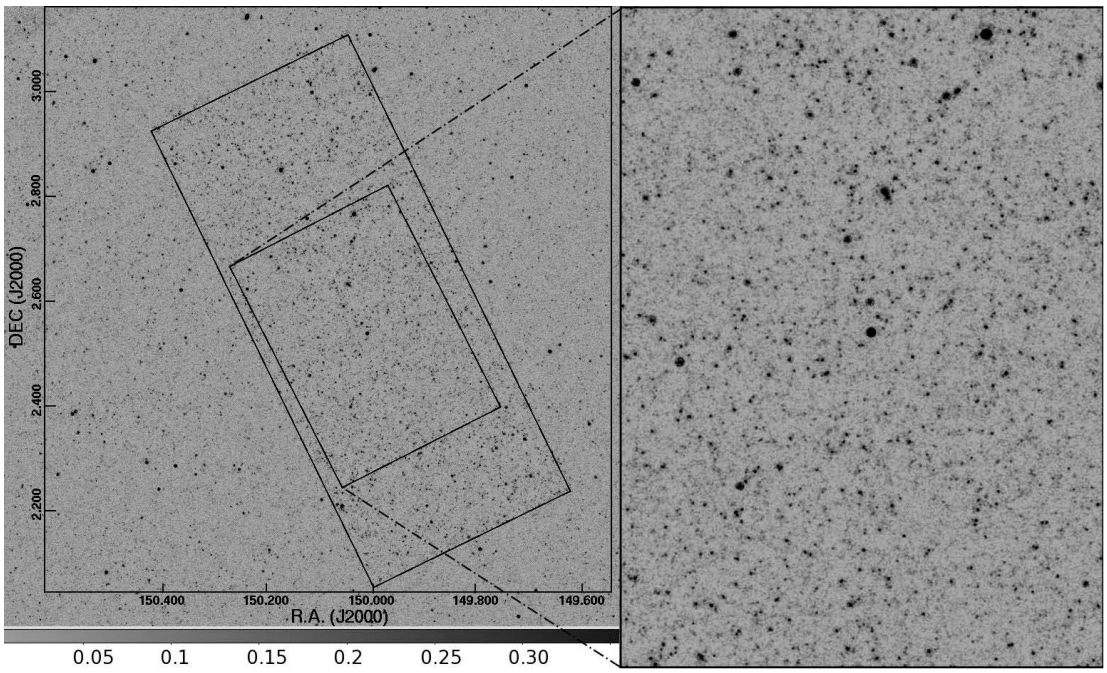

FIG. 5.—MIPS 24 μm sources in the MIPS-deep test area and larger shallow regions of the S-COSMOS field. The large rectangle (*left*) represents the full Cycle 2 deep coverage area at 24 μm, The smaller rectangle (*left*) and zoom (*right*) represent the Cycle 2 area with deep coverage in all three MIPS bands. The intensity scale bar is in units of mJy.

The variations in this background are very smooth, and therefore do not induce any kind of structure. It was possible to fit and subtract out this background using a low-order polynomial that would preserve any type of finely structured cirruslike emission from the ISM. The resulting image is shown in Figure 5. No cirruslike structure can be seen in the main or deep map. We will now quantify this statement by analyzing the power spectrum of our maps. These are computed following the prescriptions of Miville-Deschênes et al. (2002).

Gautier et al. (1992) have shown that the power spectrum of the cirrus emission of the ISM at 100 μm can be approximated by the equation

$$P(k) \propto B^2_{100\mu\mathrm{m}} \left(\frac{k}{k_0}\right)^{-3}, \tag{1}$$

where k and k_0 are spatial frequencies, $B_{100\ \mu\mathrm{m}}$ is the ISM surface brightness at 100 μm in units of Jy sr^{-1}, and $P(k)$ is the power spectrum in units of Jy^2 sr^{-1}. Note that while the original Gautier et al. (1992) formula had a dependency of $B^3_{100\ \mu\mathrm{m}}$, recent results show that $B^2_{100\ \mu\mathrm{m}}$ is a better representation below a surface brightnesses of 10 MJy sr^{-1} (Ingalls et al. 2004). From this behavior, Helou & Beichman (1990) have shown that the noise fluctuations due to infrared cirrus in a resolution element are

$$\frac{N}{1\ \mathrm{mJy}} = 0.3\left(\frac{\lambda}{100\ \mu\mathrm{m}}\right)^{2.5}\left(\frac{D_t}{1\ \mathrm{m}}\right)^{-2.5}\left(\frac{\langle B_\lambda\rangle}{1\ \mathrm{MJy\ sr^{-1}}}\right)^{1.5} = \sqrt{P(k)\Omega}, \tag{2}$$

where λ is the wavelength of observations, D_t is the telescope diameter, $\langle B_\lambda\rangle$ is the average surface brightness of interstellar dust emission at the wavelength of observations, and Ω is the measurement aperture solid angle. The predicting power of this formula has been verified to be within a factor of 2 by Kiss et al. (2001) using ISOPHOT observations. In the S-COSMOS field, we have $\langle B_{100\ \mu\mathrm{m}}\rangle = 0.9$ MJy sr^{-1} from the Schlegel et al. (1998) analysis of the *IRAS* maps. Using typical cirrus colors from Ingalls et al. (2004), we infer that the contribution of cirrus to the confusion is expected to be of $N = 0.1$ μJy at 24 μm, well below the detection limit of the deep test field. This is illustrated in Figure 6, where the power spectra of the main and deep test areas are plotted in red and green, respectively. Both spectra are dominated above 1 arcmin^{-1} by the convolution with the *Spitzer*-MIPS point spread function (PSF) that shows an exponential decrease

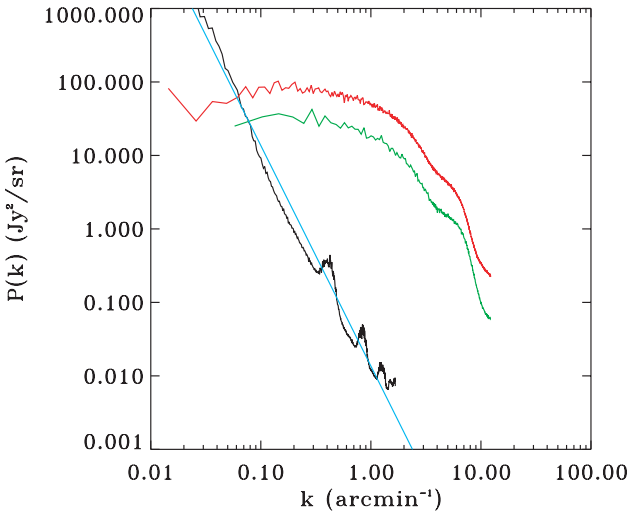

FIG. 6.—Power spectrum at 24 μm in the S-COSMOS area. *Red line*, power spectrum computed on the MIPS-shallow 24 μm image; *green line*, power spectrum computed in the MIPS-deep test area; *black line*, power spectrum computed on the *IRAS* 100 μm Schlegel et al. (1998) image (see Fig. 1), and scaled to 24 μm using eq. (1); *cyan line*, expected power spectrum from eq. (2), assuming a power law with exponent -3. Both estimations of the cirrus contribution to the power spectrum are in good agreement, and orders of magnitude below the measured power spectrum in the maps, except at the largest scales.

TABLE 3
S-COSMOS (Cycle 2) Integration Times and Measured Sensitivities

Camera	Band (μm)	Coverage (% field)	Integration Time[a] (s)	5 σ (mJy)
IRAC	3.6	100	1200	0.0009
	4.5	100	1200	0.0017
	5.6	100	1200	0.0113
	8.0	100	1200	0.0146
MIPS-shallow	24	100	80	0.42
	70	100	40	34.0
	160	100	8	150.0
MIPS-deep	24	8	3200	0.071
	70	8	1560	7.5
	160	8	320	70.0

[a] Median effective integration time per pixel.

in the power at small scales. Note also that the average ISM emission between the main and deep components is slightly different, resulting in a difference of overall power-spectrum normalization between the two areas. The black curve in Figure 6 is the power spectrum measured on the Schlegel et al. (1998) *IRAS* 100 μm, scaled to 24 μm using the square of the color ratio, $S(100\ \mu\text{m})/S(24\ \mu\text{m})$, from Ingalls et al. (2004) as shown in equation (1). At 100 μm, the *IRAS* map, very similar to the one displayed in Figure 1, is dominated by the cirrus structure. Indeed, its power spectrum is very close to a power law with index -3. By transferring it at 24 μm, we obtain an approximation of the power spectrum of the cirrus component in our map. Another approximation, given by equation (2), gives the rms fluctuations for $k = 10.3$ arcmin^{-1} in the case of *Spitzer*-MIPS 24. Assuming a power law with index -3, we obtain the cyan curve in Figure 6. Note that we did not convolve the black and cyan curves with the *Spitzer*-MIPS PSF. Doing this would introduce a further exponential decrease toward high k-values as seen in those measured on the maps. Both approximations are in extremely good agreement, and we can readily see that the cirrus emission is negligible in the field except at the largest scales. Note that the polynomial fitting we applied to subtract the zodiacal background has suppressed the largest scales of the map, which are possibly dominated by the cirrus spectrum below $k = 0.07$ arcmin^{-1}. The main conclusion from this power-spectrum analysis is that the cirrus emission is negligible at all scales except for the largest map in the field: its contribution is orders of magnitude below that of the sources in the field.

Uncertainty maps for both the main and deep observations were produced along the field mosaic. We checked the uncertainty values produced by the S13.2 pipeline at the BCD level by producing difference images of overlapping scan legs. These images were used to detect moving objects (see § 5.3). We checked the distribution of pixels in the difference images and found that the BCD product uncertainties were overestimated by 44%. We corrected all BCD uncertainty products for this factor before producing the mosaic. Final sensitivities were derived from the uncertainty maps, assuming a point source and using the point response function (PRF) produced by the SSC for MIPS 24 μm.

The MIPS-70 and MIPS-160 data were reduced using the online SSC BCD products following the pipeline algorithms presented in Gordon et al. (2005) and the filtering techniques of Frayer et al. (2006a). We have adopted the S13 calibration factors (based on stellar SEDs) of 702 and 44.7 MJy sr^{-1} per MIPS-70 and MIPS-160 units, respectively, and have applied the appropriate color corrections of 1.09 and 1.04 at 70 and 160 μm, respectively, to correct for galaxy SEDs. With future optimized processing (e.g., Frayer et al. 2006b), we hope to improve on the current S-COSMOS 70 and 160 μm sensitivities (Table 3).

5. PRELIMINARY ANALYSIS: S-COSMOS (CYCLE 2)

5.1. *Backgrounds and Sensitivities*

From our recently completed Cycle 2 observations, we validated the quality of the field for future deep-infrared observations. As shown in Table 2, we found total background levels of 37, 10.5, and 7.5 MJy sr^{-1} in the MIPS 24, 70, and 160 μm bands, respectively. The background is dominated by the zodiacal background at 24 and 70 μm and is remarkably smooth over the entire COSMOS field. In addition, no strong cirrus structures were observed within the field, as demonstrated by our power-spectrum analysis of the 24 μm maps. The zodiacal background level is $\sim$1.8–2 times higher than the low-background fields on the sky such as the Lockman Hole (LH), CDF-S, HDF-N, and the Groth Strip, which all have similar backgrounds (see Lonsdale et al. 2003 and Table 2).

For an equal amount of integration time, the S-COSMOS MIPS sensitivities at 24 and 70 μm are within 35% of the lowest background fields, confirming that the MIPS sensitivities scale as expected with the square root of the background. At 160 μm, the COSMOS field has a background level only 15% higher than the low-background fields (only 7% lower sensitivity for the same integration time). Our Cycle 2 MIPS observations of the full field (shallow) and the test area (deep) (see Table 3) show that we are able to integrate down as $\sigma \propto t^{-0.5}$. This demonstrates our ability to achieve our expected sensitivities in the MIPS-deep observations of the full field to be carried out in Cycle 3.

A complete accounting of the measured sensitivities for our Cycle 2 IRAC and MIPS observations of the COSMOS field is given in Table 3.

5.2. *Preliminary Number Counts*

5.2.1. *IRAC Number Counts*

A photometric catalog has been obtained using the IRAC 3.6 μm mosaic. The source extraction has been performed using the SExtractor software (Bertin & Arnouts 1996). Poor image quality areas have been masked (e.g., field boundary, a low-coverage area on the southwest corner,[29] areas around saturated stars). The final "effective" area (i.e., after removing the masked regions) is 2.3 deg^2.

Preliminary IRAC galaxy number counts are shown in Figure 7. The number counts shown are the number of discrete objects detected by SExtractor in the mid-infrared per flux per area. Due to the comparably large IRAC beam, comparison with extremely deep Subaru optical images indicates a significant difficulty in cross-identification between the optical images and the infrared images, which affects between 20% and 30% of the IRAC sources. However, what is shown here are strictly infrared number counts. Overall, the counts show broad agreement with those taken from elsewhere in the literature, demonstrating that the preliminary catalog is substantially free of significant systematics relative to pre-existing *Spitzer* surveys. The S-COSMOS survey is extremely deep, and photometrically reaches below the classical confusion level of 40 beams per source at 3.6 and 4.5 μm.

[29] IRAC coverage of the southwest corner of the COSMOS field was partially affected by the loss of nine AORs due to satellite transmission difficulties during our Cycle 2 observations; these AORs were scheduled to be recovered in 2006 December.

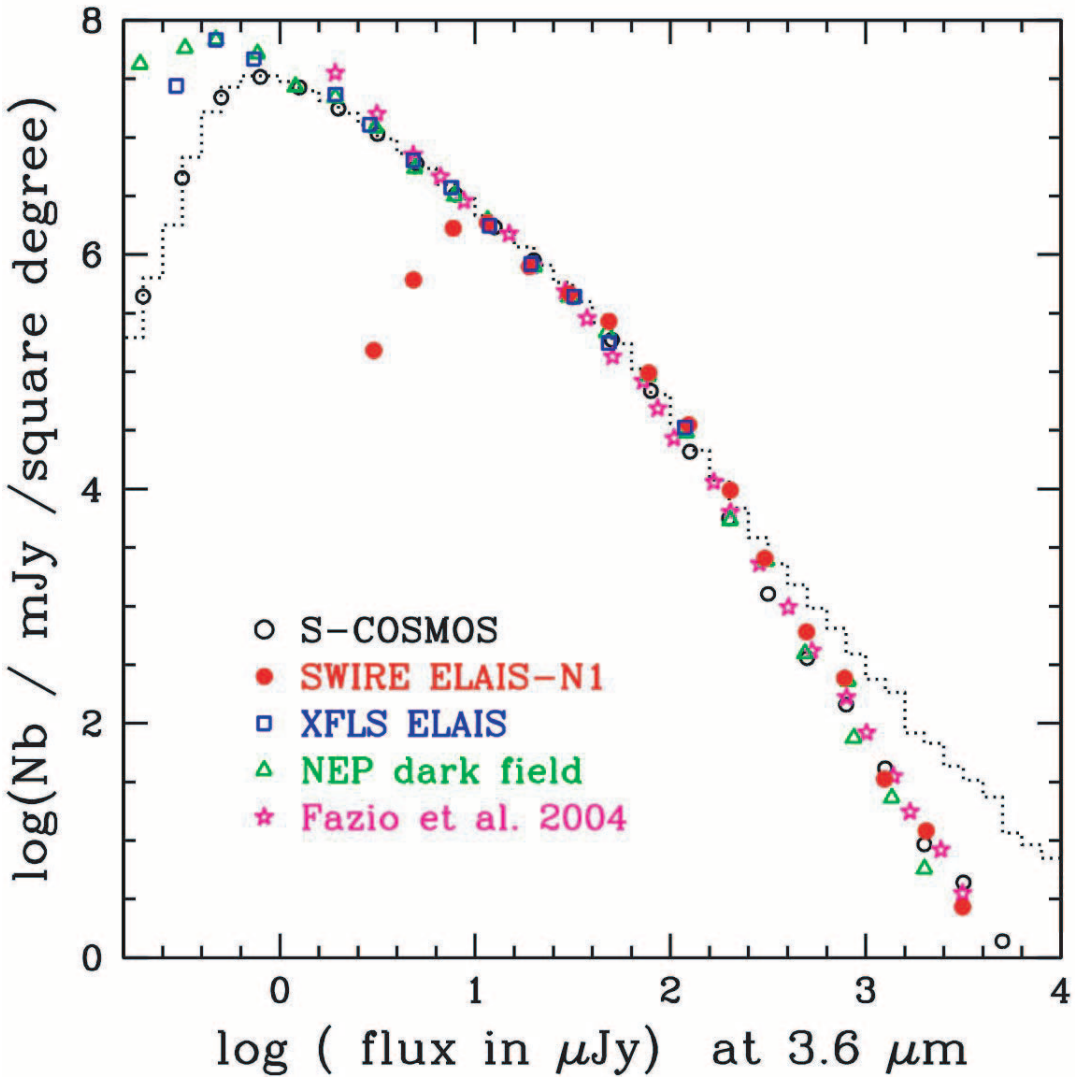

FIG. 7.—Differential number counts at 3.6 μm (IRAC-1) for the full-field Cycle 2 S-COSMOS observations. The stars are removed out to $i'_{AB} < 23$ by using a morphological criterion, FWHM/surface brightness, as measured in the *HST* ACS image (Capak et al. 2007). Given that AGNs appearing as quasi-stellar objects could also be removed by this criterion, we checked and found that X-ray-selected AGNs represent only 2% of the removed population; thus, adding them back to the galaxy sample has only a small impact on the galaxy number counts. Black open circles and the dotted line represent the S-COSMOS counts without and with the stars, respectively (see text). The SWIRE ELAIS-N1, XFLS ELAIS, and NEP dark field data are from J. A. Surace et al. (2007, in preparation). None of the number counts have been corrected for incompleteness.

As a result, confusion is significant at faint levels, and this ultimately limits the completeness of the counts at levels <1 μJy. Below this level, the number counts are systematically underestimated. Because source confusion is significant even at the total integration time of S-COSMOS, deeper surveys, e.g., IRAC North Ecliptic Pole Dark Field (Surace et al. 2004), XFLS ELAIS-N1 (Fadda et al. 2004; Rodighiero et al. 2006), and QSO HS 1700+6416 (Fazio et al. 2004; Barmby et al. 2004), do not extend to proportionally fainter levels. Thus, while S-COSMOS is $\sim$50 times shallower in integration time than those deeper surveys, it reaches similar flux levels while covering an area between 40 and 200 times larger. Thus, S-COSMOS is as effective as any existing *Spitzer* survey for studying faint galaxy populations, but at the same time minimizes cosmic variance on 1° scales when studying those populations due to its larger area. Surveys such as SWIRE will provide more information on cosmic variance for brighter sources due to both the larger total area coverage (25 times), and sampling more (by a factor of 6) fields. However, the SWIRE completeness limit is more than 10 times brighter than that of S-COSMOS, and therefore cannot address the faintest decade in flux.

5.2.2. *MIPS Number Counts*

A preliminary catalog has been extracted from the full-field shallow and deep test area images. Source detection has been performed using the IDL version of the DAOPHOT (Stetson 1987) on the S/N ratio images. This method has been found to be the most efficient in separating the high ($\sim$25%) fraction of blended sources in the deep area where the depth reaches below 70 μJy. Source fluxes were measured on the images using aperture photometry, masking out neighboring sources that could contribute significantly. They were then scaled to total fluxes, using the MIPS 24 μm PRF provided by the SSC, and taking the masked pixels into account. This method allows us to deal with the blending in a preliminary way.

Stars were identified using both the Robin et al. (2007) catalog derived from ACS morphology and the 2MASS PSC catalog (Skrutskie et al. 2006) for the bright end. In addition, we checked

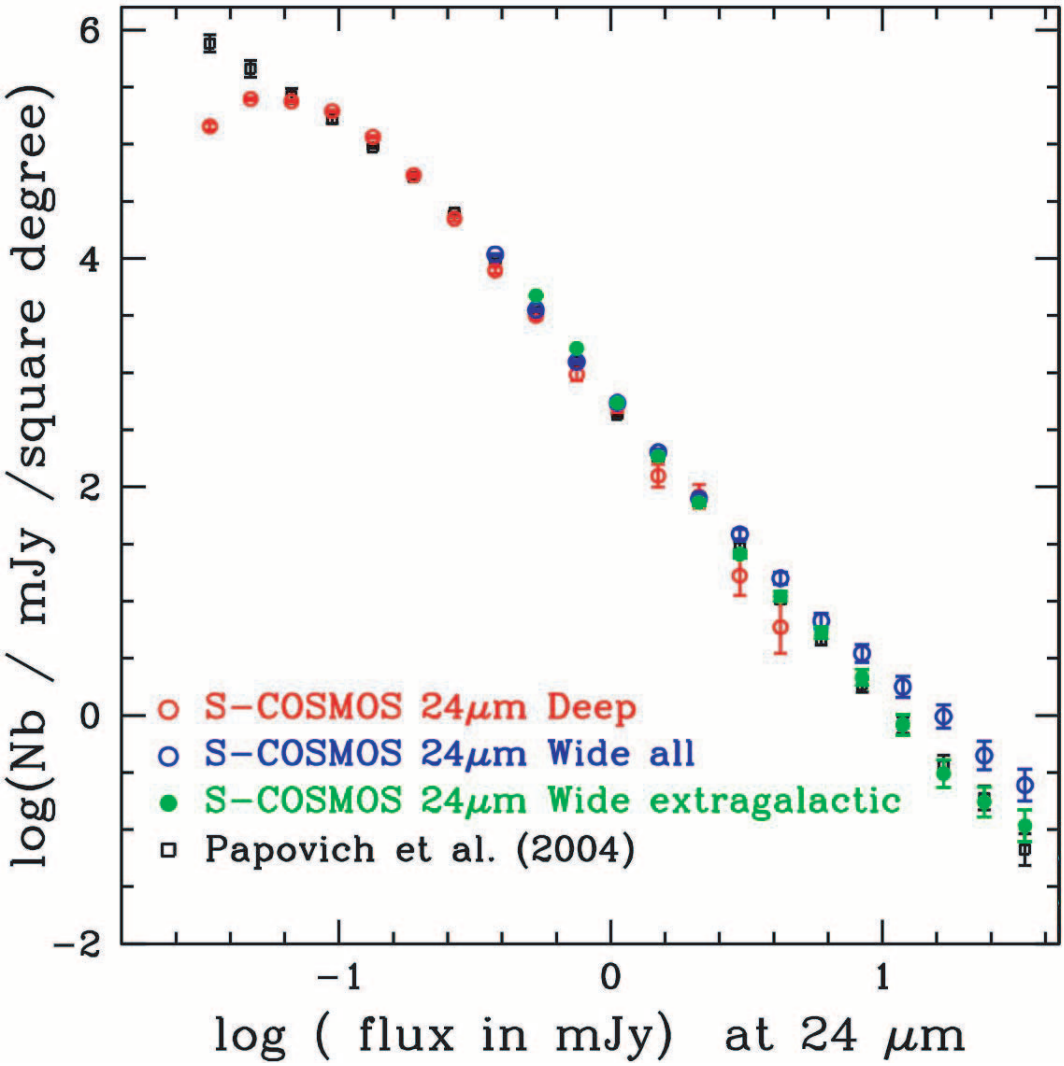

FIG. 8.—Preliminary differential counts at 24 μm from the MIPS-deep test area (*red open circles*) and MIPS-shallow "wide all" (*cyan open circles*) Cycle 2 S-Cosmos observations, compared to those compiled by Papovich et al. (2004). The error bars for the S-COSMOS counts are the 1 σ Poissonian fluctuations. The counts in the MIPS-deep area are compatible with the Papovich counts (*squares*) down to our 5 σ completeness limit of 67 μJy. In the MIPS-shallow "wide all" observations, the excess of sources detected at large fluxes is due to stars in the field. The MIPS-shallow "wide extragalactic" (*green filled circles*) counts were obtained after removal of the stars (see text).

against our *XMM-Newton* point-source catalog in order to avoid including any AGNs among the starlike objects. We find that stars account for roughly 5% of the MIPS 24 μm detections at 1 mJy. This fraction rises to 50% at the bright end of the counts.

The number counts for both the S-COSMOS full-field MIPS-shallow and MIPS-deep test area images are displayed in Figure 8, together with the results from the guaranteed time observation (GTO) surveys compiled by Papovich et al. (2004). The counts from the deep area agree well at their bright end with the ones from the full field at their faint end. They also agree within the Poisson error bars with the GTO counts. The effect of stellar contamination is clearly visible in the counts on the MIPS-shallow area where both the counts with and without the inclusion of stars is shown.

5.3. *Asteroids*

In the context of number counts, asteroids are considered a contaminant and are masked in the final image. On the other hand, *Spitzer* is ideally suited to study the thermal emission of asteroids, especially of main belt asteroids (MBAs), whose peak flux is typically measured at 15–20 μm. Understanding the current size frequency distribution (SFD) of the MBA population provides important insights into the evolution of the solar system, including accretion and collisional history, as well as impact hazards to the Earth. Although Tedesco et al. (2005) have suggested that the MBA population is composed of a significant fraction of smaller (subkilometer-diameter) objects, these bodies have only been observable since the launch of *Spitzer*. Their Figure 6, based on ground-based observations of $\sim 1.9 \times 10^6$ known asteroids and extrapolation of the SFDs of several asteroid families, suggests that the number of objects increases logarithmically with decreasing diameter. The actual number of smaller objects has been difficult to empirically determine, however, as MBAs emit most of their radiation in the mid-IR, leading to observational bias toward larger, more reflective asteroids.

Figure 9 shows the observed optical and IR SED of asteroid MBA 248, viewed at heliocentric and *Spitzer*-centric distances of 2.63 and 1.62 AU, respectively. The optical and IR emission

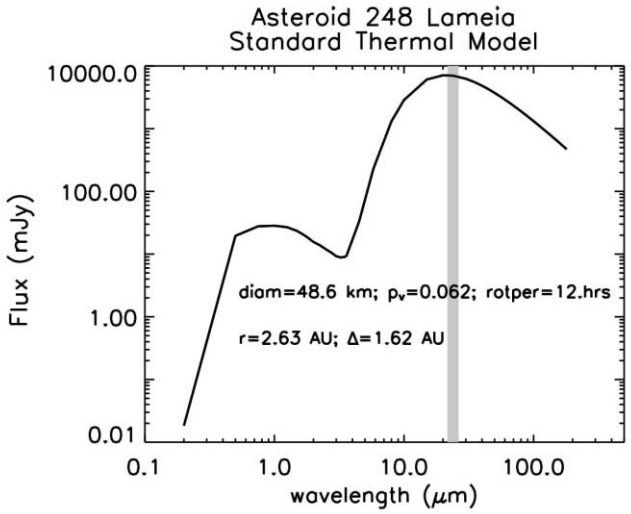

FIG. 9.—Model spectral energy distribution for main belt asteroid 248 Lameia. The standard thermal model, assuming geometric albedo $pv = 0.062$ is used. As this object is highly nonreflective, the mid-IR emission is 2 orders of magnitude greater than at optical wavelengths. The gray bar represents the MIPS 24 μm band. This object's thermal properties are similar to those of other MBAs, making them ideally suited for detection at the S-COSMOS wavelengths of 8 and 24 μm.

is from reflected sunlight and thermal emission, respectively. The MBA 248 SED can be considered typical of asteroid SEDs at these wavelengths. As predicted by the widely used so-called "Standard Thermal Model" (Lebofsky & Spencer 1989), these solar system bodies are expected to emit substantially more radiation in the mid-IR than at optical wavelengths, thus making ground-based detection feasible for only a subset of the MBA population.

S-COSMOS, carried out near the ecliptic plane at $\beta \sim -9^\circ$, has detected more than 120 asteroids deg^{-1} at 24 μm, down to a sensitivity limit of 0.30 mJy (5 σ), in the Cycle 2 MIPS-deep test area (see examples in Figure 10). For comparison, the only *Spitzer* asteroid survey carried out to date, the First Look Survey Ecliptic Plane Component (FLS-EPC), has looked at number counts in the ecliptic plane (i.e., $\beta \sim 0^\circ$) from 8 μm IRAC observations down to a sensitivity limit of 0.08 mJy (5 σ), and these data indicate that 125 ± 33 asteroids deg^{-1} are present.

Because the SFD for the MBA population is expected to change with distance from the ecliptic plane (Brooke et al. 2003), and the sensitivity limits of the two programs are different, a direct comparison between S-COSMOS and FLS-EPC asteroid number counts cannot be made. The FLS-EPC has shown that the asteroid mid-IR color, $S(24\ \mu\text{m})/S(8\ \mu\text{m})$, appears to be constant over a large range of diameters and albedos (Bhattacharya et al. 2004; Meadows et al. 2004), and this result can be used to reconcile the two data sets. As the FLS-EPC suggests that $S(24\ \mu\text{m})/S(8\ \mu\text{m}) \sim 10$ down to a sensitivity limit of $\sim$0.08 mJy (5 σ), a relevant comparison to S-COSMOS MIPS-deep test area asteroids should only be made for objects with $S(24\ \mu\text{m}) \geq 0.8$ mJy, with latitudinal drop-off modeled by a power law (Cellino et al. 2001). As part of our future work, we plan to carry out this analysis, as well as a detailed photometric analysis and thermal modeling, to refine the overall number counts as discussed above, as well as to refine color values and to determine orbits. It is anticipated that the Cycle 3 MIPS-deep observations of the full COSMOS field will detect $\sim$12 times the number of asteroids found in the Cycle 2 MIPS-deep test area, thus reducing the uncertainty in the preliminary number counts per square degree provided here.

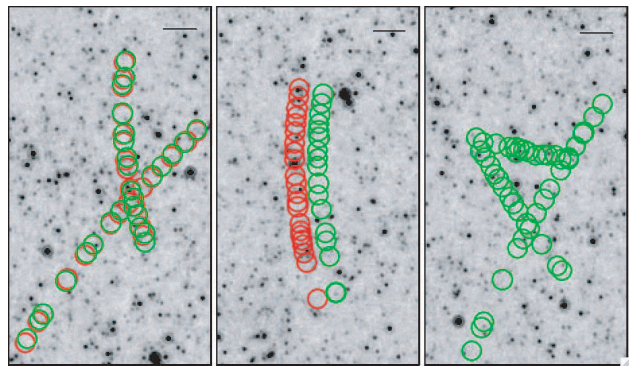

FIG. 10.—Example of asteroids and their trajectories on the deep MIPS 24 μ image. The figure has the asteroids removed. Green circles reflect the positions of the asteroids before removal. We queried the JPL Horizons On-Line Ephemeris Service using a *Spitzer*-centric line of sight (http://ssd.jpl.nasa.gov/x/ispy.html) in order to quantify the number of asteroids already known. Red circles reflect expected locations for the asteroids based on these queries. Less than 20% are known to the system (*left, middle*) while 80% are new detections (*right*). Among the asteroids already known, some have a trajectory that is only approximately known; therefore an offset is measured when compared with our detections (*middle*). The scale bar in the upper right of each panel represents 1′.

6. DATA QUALITY AND FUTURE SCIENCE GOALS

The preliminary results from our S-COSMOS Cycle 2 IRAC and MIPS observations have confirmed expectations that the COSMOS field is one of the best equatorial fields of comparable size available for carrying out deep-infrared surveys. Our preliminary analysis has demonstrated that (1) the full COSMOS field is devoid of cirrus contamination, (2) we are able to achieve our predicted sensitivities with both IRAC and MIPS cameras within the allotted integration times, (3) measured background levels were very close to those predicted, demonstrating our ability to minimize the zodiacal background levels through judicious use of the visibility windows, and (4) our observing methods allow for efficient removal of asteroid "contaminants," and in fact have resulted in the discovery of many new main-belt asteroids.

The IRAC and MIPS sensitivities achieved in Cycle 2 (and expected for Cycle 3 MIPS) will allow us to carry out the two main science goals of S-COSMOS: a study of the stellar mass assembly of galaxies and a full accounting of the luminosity from dust-embedded sources such as merging starburst galaxies and AGNs, primarily in the redshift range $z \sim 0.5$–3, where COSMOS is designed to study galaxy evolution as a function of large-scale structure environment and redshift (Scoville et al. 2007).

An estimate of the numbers of galaxies that will be detected by S-COSMOS can be made using the SEDs shown in Figure 11, along with the local luminosity function (LF) for infrared-selected galaxies (e.g., Sanders et al. 2003) and a model for evolution of the LF with redshift (e.g., Kim & Sanders 1998; Sanders 2003). Figure 11 shows four redshifted galaxy SEDs together with the measured sensitivities for the S-COSMOS and *HST* ACS surveys. Included are a massive bulge-dominated system ("M87-like"), an actively star-forming disk ("M51-like"), and both "cool" and "warm" ultraluminous IR/merging systems (e.g., Arp 220, Mrk 231) with varying mixtures of starburst and AGN activity. Our integration time of $\sim$1200 s pixel^{-1} in each of the four IRAC bands is sufficient to easily detect $\sim L^*$ disks and spheroids out to $z \sim 3$. The total number of objects detected by IRAC over the full COSMOS is expected to be $\gtrsim 10^6$ as determined from the differential number counts at 3.6 μm (see Fig. 7). The MIPS-deep integration times of $\sim$3000 s at 24 μm will allow

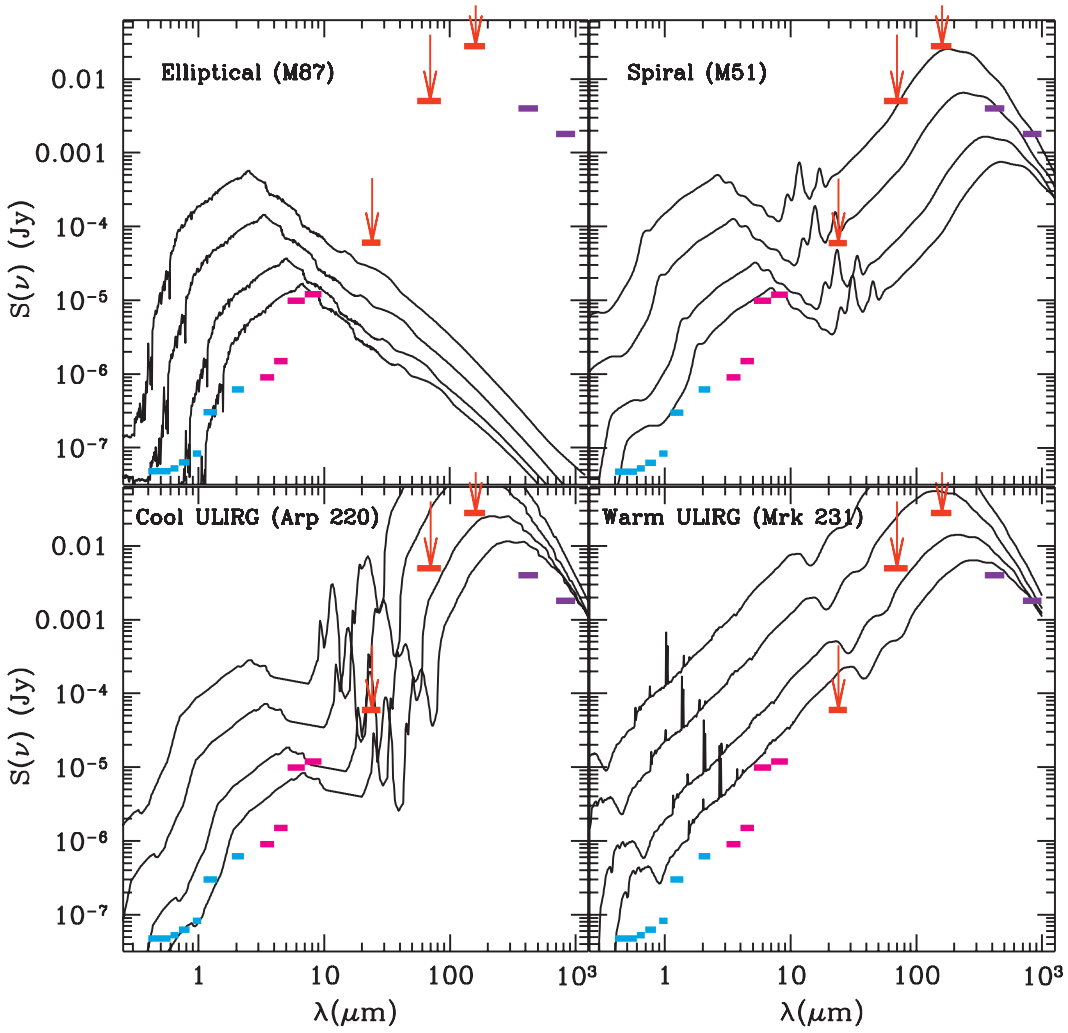

FIG. 11.—SEDs of galaxies (Franceschini et al. 2001), as a function of $z = 0.5, 1, 2, 3$ (*solid curves, top to bottom*). The elliptical ("M87-like") and spiral ("M51-like") templates have been scaled to $L_{\rm bol} = 10^{11}$ and $3 \times 10^{11}\ L_{\odot}$, respectively. The "cool" and "warm" ULIRG templates have been scaled to $L_{\rm bol} = 2 \times 10^{12}\ L_{\odot}$. Superimposed in color are S-COSMOS and COSMOS survey sensitivities (5 σ): *red arrows*, S-COSMOS Cycle 2 MIPS-shallow survey (this paper); *red bars*, Cycle 2 MIPS-deep survey (this paper); *magenta bars*, S-COSMOS Cycle 2 IRAC survey (this paper); *blue bars*, COSMOS ground-based, optical/NIR (*BVr′i′z′JK*) data (Capak et al. 2007; Taniguchi et al. 2007). The purple bars at 450 μm and 850 μm show the expected sensitivities (5 σ) from our recently approved University of Hawaii + Tri-national Legacy survey of the COSMOS field with JCMT SCUBA2 (Holland et al. 2003).

us to detect luminous infrared galaxies (LIRGs: $L_{\rm IR} > 10^{11}\ L_{\odot}$) out to $z \sim 2$, and ultraluminous infrared galaxies (ULIRGs: $L_{\rm IR} > 10^{12}\ L_{\odot}$) out to $z \sim 3$. To compute the total number of objects expected to be detected by MIPS, we have assumed strong evolution of the form $(1+z)^{5.5}$ for objects with $L_{\rm IR} \gtrsim 3 \times 10^{11}\ L_{\odot}$, consistent with the strong evolution either measured or inferred from previous studies (e.g., Sanders 2003; Oyabu et al. 2005; Le Floc'h et al. 2005), which show that the comoving space density of the LIRG/ULIRG population appears to increase by 2–3 orders of magnitude over the redshift range 0–2. At 24 μm, S-COSMOS should detect $\gtrsim 10^5$ LIRGs out to $z \sim 2$ and $\gtrsim 3 \times 10^3$ ULIRGs out to $z \sim 3$–4. At 70 and 160 μm, S-COSMOS should detect $\sim 10^3$ ULIRGs out to $z \sim 1.5$–2.

S-COSMOS is optimal for selecting unbiased samples of AGNs almost independently of their level of obscuration. At mid-infrared wavelengths the obscuring dust that hides AGNs from ultraviolet, optical, and soft X-ray surveys should be a strong and largely isotropic emitter. As shown by Lacy et al. (2004) and Stern et al. (2005) and references therein, selection based on mid-IR colors (specifically, IRAC and MIPS colors from 3.6 to 24 μm) can not only help disentangle stars, galaxies, and AGNs, but also help separate type 1 and type 2 AGNs using the same criteria. This is crucial if one wants to quantify the ratio of type 2 to type 1 AGNs in the universe. In fact, obscuration models that aim to resolve the hard (>8 keV) X-ray background (XRB) debate whether the ratio remains constant during AGN evolution (e.g., Treister & Urry 2005), or whether it varies as a function of redshift and luminosity (e.g., Gilli et al. 2006). Thus, the COSMOS field, with its size, deep mid-IR coverage, and extensive UV, X-ray, radio, and optical data sets offers not only the possibility of significantly improving the constraint on the surface density of obscured AGNs, but also of improving our understanding of their spectral energy distributions (SEDs), and hence the ratio of type 2 to type 1 AGNs.

The S-COSMOS data will be combined with the full multiwavelength COSMOS data set to compute fundamental properties of galaxies. IRAC+MIPS data will provide a much more complete accounting of the bolometric luminosity, particularly for luminous starbursts and dusty AGNs. In addition, the combination of IRAC (e.g., 5–8 μm) and MIPS (e.g., 24 μm) data

will be essential in order to provide a useful discriminant between starburst and AGN activity (e.g., Rigby et al. 2004; Prouton et al. 2004; Stern et al. 2005). The S-COSMOS IRAC and MIPS colors can also be used as an AGN versus star formation discriminator in faint radio sources (Schinnerer et al. 2007). Once a galaxy has been identified as actively forming stars, the combination of radio and *Spitzer* data, as well as the relatively accurate photometric, and in some cases spectroscopic redshifts, will be used to both calibrate and determine the cosmic evolution of the radio-FIR correlation for star-forming galaxies. The S-COSMOS observations will also be combined with the deep radio and (sub)millimeter observations of the COSMOS field to determine accurate radio through rest-frame far-infrared SEDs of the submillimeter galaxies in the COSMOS field (Bertoldi et al. 2007). These observations will provide the best constraints to date on the physical conditions in the submillimeter galaxies (e.g., dust temperatures, dust masses, and bolometric luminosities).

The S-COSMOS data will also be used to select different populations of new and interesting objects for further study. For example, using our IRAC S-COSMOS data in combination with our optical and near-infrared COSMOS data, ULIRGs can be effectively selected by the *BzK* criterion up to $z \sim 2.5$ (Daddi et al. 2005), whereas a similar criterion based on the *RJL* bands (exploiting the IRAC 3.5 μm data from S-COSMOS) will expand the selection of these objects up to $z \sim 4$ (Daddi et al. 2004). Also, for a typical Type 1 AGN SED, both our IRAC and MIPS S-COSMOS observations will detect objects with optical luminosity 1.5×10^{44} ergs s^{-1}, 20 times fainter than the mean luminosity of SDSS QSOs at a typical redshift of $z = 1.5$ (Richards et al. 2006).

It is clear that S-COSMOS will provide a critical part of the overall COSMOS study of galaxy evolution at $z \sim 0.5$–3, particularly at $z > 1$, where luminous infrared galaxies become a dominant population of extragalactic objects. Interactions and mergers are very likely responsible for driving the strong evolution seen in the LIRG/ULIRG population over the redshift range $z \sim 0$–2 (e.g., Sanders 2003; Le Floc'h et al. 2005; Babbedge et al. 2006), and therefore galaxy environment will almost certainly play a prominent role in triggering these systems (Kauffmann et al. 2003, 2004). One of the primary goals of S-COSMOS will be to explore the role of environment in producing the LIRG/ULIRG population at $z = 0.5$–2.5 and, using *HST* imaging, to determine the galaxy types involved in the process.

The S-COSMOS Cycle 2 MIPS and IRAC reduced images and catalogs became publicly available in 2007 May, while the Cycle 3 MIPS reduced images and catalogs will be made public in 2008 June, one year after the final S-COSMOS Cycle 3 MIPS observing campaign. A more complete description of the data release products and timeline can be found on the *Spitzer* Legacy Program Web page.[30]

This work is based on observations made with the *Spitzer Space Telescope*, which is operated by the Jet Propulsion Laboratory (JPL), California Institute of Technology under NASA contract 1407. Support for this work was provided by NASA through contract 1278386 issued by the JPL. It is a pleasure to acknowledge the hospitality provided by the Aspen Center for Physics where the majority of this paper was written. Additional information on the S-COSMOS Legacy Survey is available from the main COSMOS Web site at http://www.astro.caltech.edu/cosmos. It is a pleasure to acknowledge the excellent services provided by the NASA IPAC/IRSA staff (Anastasia Laity, Anastasia Alexov, Bruce Berriman, and John Good) in providing online archive and server capabilities for the COSMOS data sets. We thank Guilaine Lagache for useful comments on power spectra measurements. We would also like to thank the referee for comments and suggestions which helped clarify our presentation.

Facilities: HST (ACS), Spitzer (IRAC), Spitzer (MIPS)

[30] http://ssc.spitzer.caltech.edu/legacy/all.html.

REFERENCES

Babbedge, T. S., et al. 2006, MNRAS, 370, 1159
Barmby, P., et al. 2004, ApJS, 154, 97
Bertin, E., & Arnouts, S. 1996, A&AS, 117, 393
Bertoldi, F., et al. 2007, ApJS, 172, 132
Bhattacharya, B., et al. 2004, BAAS, 204, 721
Brooke, T., et al. 2003, Main Belt Asteroids in Spitzer Observations (Pasadena: Caltech), http://ssc.spitzer.caltech.edu/documents/asteroid_memo.pdf
Capak, P., et al. 2007, ApJS, 172, 284
Cellino, A., Zappala, V., & Farinella, P. 2001, MNRAS, 253, 561
Daddi, E., Cimatti, A., Renzini, A., Fontana, A., Mignoli, M., Pozzetti, L., Tozzi, P., & Zamorani, G. 2004, ApJ, 617, 746
Daddi, E., et al. 2005, ApJ, 631, L13
Fadda, D., Jannuzi, B.T., Ford, A., & Storrie-Lombardi, L. J. 2004, AJ, 128, 1
Fadda, D., et al. 2006, AJ, 131, 2859
Fazio, G. G., et al. 2004, ApJS, 154, 39
Franceschini, A., Aussel, H., Cesarsky, C. J., Elbaz, D., & Fadda, D. 2001, A&A, 378, 1
Frayer, D. T., et al. 2006a, AJ, 131, 250
———. 2006b, ApJ, 647, L9
Gautier, T. N., III, Boulanger, F., Perault, M., & Puget, J. L. 1992, AJ, 103, 1313
Gilli, R., Comastri, A., & Hasinger, G. 2006, in The X-Ray Universe, ed. A. Wilson (ESA SP-604), 813
Gordon, K. D., et al. 2005, PASP, 117, 503
Helou, G., & Beichman, C. A. 1990, in From Ground-Based to Space-Borne Sub-mm Astronomy, (SEE N91-21986 13-89; Garching: ESA), 117
Holland, W. S., Duncan, W., Kelly, B. D., Irwin, K. D., Walton, A. J., Ade, P. A. R., & Robson, E. I. 2003, Proc. SPIE, 4855, 1
Impey, C., et al. 2007, submitted
Ingalls. J. C., et al. 2004, ApJS, 154, 281
Kampczyk, P., et al. 2007, ApJS, 172, 329
Kartaltepe, J. S., et al. 2007, ApJS, 172, 320
Kauffmann, G., White, S. D. M., Heckman, T. M., Ménard, B., Brinchmann, J., Charlot, S., Tremonti, C., & Brinkmann, J. 2004, MNRAS, 353, 713
Kauffmann, G., et al. 2003, MNRAS, 346, 1055
Kim, D.-C., & Sanders, D. B. 1998, ApJS, 119, 41
Kiss, C., Ábrahám, P., Klaas, U., Juvela, M., & Lemke, D. 2001, A&A, 379, 1161
Lacy, M., et al. 2004, ApJS, 154, 166
Lebofsky, L. A., & Spencer, J. R. 1989, in Asteroids II, ed. R. Binzel, (Tucson: Univ. Arizona Press), 128
Le Floc'h, E., et al. 2005, ApJ, 632, 169
Lonsdale, C. J., et al. 2003, PASP, 115, 897
Makovoz, D, Khan, I., & Moshir, M. 2005, PASP, 117, 274
Meadows, V. S., et al. 2004, ApJS, 154, 469
Miville-Deschênes, M.-A., Lagache, G., & Puget, J.-L. 2002, A&A, 393, 749
Mobasher, B., et al. 2005, ApJ, 635, 832
Oyabu, S., et al. 2005, AJ, 130, 2019
Papovich, C., et al. 2004, ApJS, 154, 70
Polletta, M., et al. 2006, ApJ, 642, 673
Prouton, O. R., Bressan, A., Clemens, M., Franceschini, A., Granato, G. L., & Silva, L. 2004, A&A, 421, 115
Richards, G. T., et al. 2006, AJ, 131, 2766
Rigby, J., et al. 2004, ApJS, 154, 160
Robin, A., et al. 2007, ApJS, 172, 545
Rodighiero, G., et al. 2006, MNRAS, 371, 1891
Rowan-Robinson, M., et al. 2005, AJ, 129, 1183
Sanders, D. B. 2003, J. Korean Astron. Soc., 36, 149
Sanders, D. B., Mazzarella, J. M., Kim, D.-C., Surace, J. A., & Soifer, B. T. 2003, AJ, 126, 1607

Schinnerer, E., et al. 2007, ApJS, 172, 46
Schlegel, D. J., Finkbeiner, D. P., & Davis, M. 1998, ApJ, 500, 525
Scoville, N. Z., et al. 2007, ApJS, 172, 1
Skrutskie, M. F., et al. 2006, AJ, 131, 1163
Stern, D., et al. 2005, ApJ, 631, 163
Stetson, P. B. 1987, PASP, 99, 191
Surace, J. A., & the SWIRE Team, 2004, BAAS, 36, 1450
Taniguchi, Y., et al. 2007, ApJS, 172, 9
Tedesco, E. F., Cellino, A., Zappalá, V. 2005, AJ, 129, 2869
Treister, E., & Urry, C. M. 2005, ApJ, 630, 115